# Prior-Guided Metal Artifact Reduction for Iterative X-Ray Computed Tomography

Zhiqian Chang, *Member, IEEE*, Dong Hye Ye, *Member, IEEE*, Somesh Srivastava, *Member, IEEE*, Jean-Baptiste Thibault, *Member, IEEE*, Ken Sauer, *Member, IEEE*, and Charles Bouman, *Fellow, IEEE*

***Abstract*— High-attenuation materials pose significant challenges to computed tomographic imaging. Formed of high mass-density and high atomic number elements, they cause more severe beam hardening and scattering artifacts than do water-like materials. Pre-corrected line-integral density measurements are no longer linearly proportional to the path lengths, leading to reconstructed image suffering from streaking artifacts extending from metal, often along highest-density directions. In this paper, a novel prior-based iterative approach is proposed to reduce metal artifacts. It combines the superiority of statistical methods with the benefits of sinogram completion methods to estimate and correct metal-induced biases. Preliminary results show minimized residual artifacts and significantly improved image quality.**

***Index Terms*— Statistical reconstruction, iterative reconstruction, metal artifact reduction, beam hardening correction, computed tomography.**

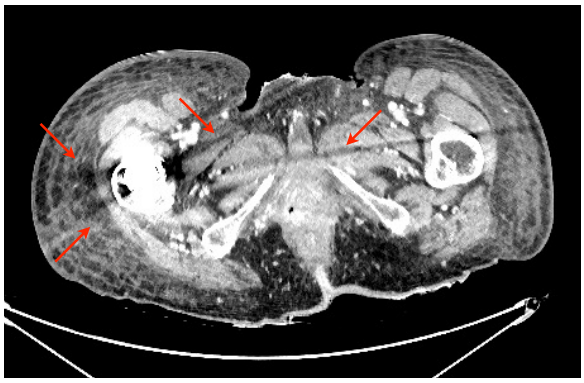

Fig. 1. Hip implant-induced metal artifacts, with water-based scatter and beam hardening correction applied. Display window [−100, 100] HU.

## I. Introduction

COMMERCIALLY common computed tomography (CT) scanners emit polychromatic X-ray beams. Measured line-integral projections, suffering from beam hardening effects [1]–[3], are consequently not linearly proportional to corresponding path-lengths. Compton scattering, as one of the principal photon attenuation mechanisms, adds nonlinearity to the line-integrals by contaminating raw photon measurements with local bias and increased quantum noise. In medical imaging systems, water-based beam hardening and scatter corrections are usually performed as data pretreatments, based on the high concentration of water-like materials (e.g., soft tissues) in human body [4], [5]. However, in the presence of high-density metal materials from dental fillings, joint replacements or other orthopaedic implants, water-based corrections become insufficient. As a result, uncorrected sinogram biases propagate into reconstructed images, degrading the diagnostic quality. For instance, as shown in Fig. 1, the metallic alloy hip replacement induces streaking and shading artifacts into nearby soft tissues and bones, interrupting the continuity and uniformity of anatomic structures.

High-density materials are usually composed of elements with high atomic numbers, which attenuate low-energy X-ray photons at much higher rates than they do those of high-energy, leading to more severe beam hardening effects than found in water. Scattering noise is also more prominent with dense materials, according to the Klein-Nishina formula [6]. With common photon detection mechanisms, beam hardening and scatter effects are often indistinguishable from each other, and therefore collectively cause metal artifacts. To reduce metal impact, composite materials with lower metal concentration or devices with smaller cross-sections are preferred [7]–[9]. A pre-filtered, high-energy X-ray spectrum can be utilized at the cost of diminishing imaging contrast [7].

More practically, metal artifact reduction (MAR) algorithms have been developed to meet the challenge [10]–[31]. A common assumption is that projections from rays passing through metal are heavily corrupted, and image reconstruction would be improved by synthetic replacement data. First proposed by Kalender *et al.* [10] (1987), sinogram completion

Manuscript received October 3, 2018; revised November 27, 2018; accepted December 10, 2018. Date of publication December 14, 2018; date of current version May 31, 2019. This work was supported by GE Healthcare. *(Corresponding author: Zhiqian Chang.)*

Z. Chang is with Intel Corporation, Hillsboro, OR 97124 USA (e-mail: zhiqian.chang@intel.com).

D. H. Ye and C. Bouman are with the Department of Electrical and Computer Engineering, Purdue University, West Lafayette, IN 47907-0501 USA (e-mail: yed@purdue.edu; bouman@purdue.edu).

S. Srivastava and J.-B. Thibault are with the Applied Science Laboratory, GE Healthcare, Waukesha, WI 53188 USA (e-mail: someshsrivastava@ge.com; jean-baptiste.thibault@med.ge.com).

K. Sauer is with the Department of Electrical Engineering, University of Notre Dame, Notre Dame, IN 46556-5637 USA (e-mail: sauer@nd.edu).

Color versions of one or more of the figures in this paper are available online at http://ieeexplore.ieee.org.

Digital Object Identifier 10.1109/TMI.2018.2886701

methods try to replace the "bad" metal projection data with interpolation [11]–[16], pattern recognition [17], or linear prediction methods [18]. Among these, normalized metal artifact reduction (NMAR), proposed by Meyer *et al.* [14] is among the most influential. It provides a two-pass framework by using the intermediate image from the first-pass sinogram in-painting to create a normalized projection space, where the second-pass interpolation may avoid abrupt transitions on metal trace boundaries. To overcome high-frequency noise patterns sometimes introduced by NMAR, a frequency-split method was used to blend it with the FBP image [19], [20]. Alternatively, material decomposition-inspired methods were proposed [21]–[23] to reduce beam hardening artifacts. These methods approximate sinogram biases with polynomials of two basis materials as data pretreatment. However, they are usually limited by the degrees of freedom when it comes to existence of multiple materials. Additionally, iterative approaches are used to estimate projection values from the "bad" sinogram data. La Rivière [24] proposed penalized-likelihood sinogram smoothing as a pre-processing method, which estimates the metal line-integrals by maximizing a penalized-likelihood objective function. A maximum likelihood expectation maximization (ML-EM) algorithm and the algebraic reconstruction technique (ART) have been modified to ignore the missing data [25], [26]. Statistical reconstruction methods are strategically advanced in dealing with metal artifacts, given the statistical data weighting and *a priori* image models [27]–[29]. Image-domain artifact correction, not dependent on availability of original sinogram data, has shown promise in estimation/segmentation for material classification from CT [30]. Recently, Jin *et al.* [31] proposed simultaneous estimation of the image and low-order polynomial coefficients for beam-hardening correction. For circumstances in which physical geometry and composition of implanted components are available, Stayman *et al.* [32] proposed a joint estimation of the component spatial pose and the anatomy of scanned object; Ruth *et al.* [33] used three-dimensional, registered computer-aided design (CAD) data as prior knowledge to improve segmentation accuracy. However, all of these methods have their limits of accuracy and/or applicability, and may not achieve consistency across varied reconstruction applications.

In this paper, we are particularly interested in metal artifact correction as a component of model-based iterative reconstruction (MBIR). Iterative approaches such as MBIR may excel at noise suppression and reduce some metal artifacts through regularization. Modeling of varying reliability of data can be used to spatially adapt fidelity to data and adherence to prior models to suppress errors. However, iterative techniques are also sensitive to system modeling errors such as departures from the linear attenuation model found in metal projections. Streaking artifacts may be attenuated relative to FBP results, but their spatial extent may persist or even be extended by MBIR's response to data inconsistencies. Thus supplemental correction of metal effects is needed beyond standard water-based methods.

Our approach is of the class of iterative algorithms which seek to extract useful information from metal traces rather than entirely replacing or dropping them from the sinogram. De Man *et al.* [34], and Slambrouck and Nuyts [35] applied a polychromatic model locally to correct beam hardening effects in an iterative reconstruction. In a similar vein, Elbakri and Fessler [36] introduced a material decomposition-based sinogram correction into the reconstruction. Srivastava and Fessler [37] and Abella and Fessler [38] reduced the correction to a function of a single material for beam hardening. These methods all require advance knowledge of X-ray spectra and material properties. Our proposed approach here has more in common with [31] in that we attempt to compensate for metal data inconsistencies by direct estimation of the biasing error as part of the reconstruction process, without information on the system or materials.

We propose an iterative reconstruction and metal artifact reduction algorithm guided by an *a priori* image relatively free of metal effects. It makes use of a reconstructed "prior" image from sinogram completion methods, and integrates this prior image into a Bayesian inference framework, where the unknown image and the metal-induced projection biases are jointly estimated. This preserves the desirable resolution improvement and noise control of MBIR along with the favorable artifact suppression of NMAR. In contrast to the method in [31], we allow a much larger number of parameters to describe the metal inconsistencies, but stabilize them with regularization. The method was applied on various phantom and clinical scan data, and compared to the state-of-the-art NMAR method. Results show appreciable improvements in image quality relative to either method alone.

## II. Description of Method

In model-based statistical reconstruction, the log-likelihood for the image $x$ may typically be described in a weighted least squares form [39], [40] as

$$\log p(y|x) \approx -\frac{1}{2}(y - Ax)^T W(y - Ax), \tag{1}$$

where the data $y \in R^M$ represents the measured projections; $A \in R^{M\times N}$ represents forward projection of the imaging system; and $W$ is a diagonal weighting matrix, with entries approximately inversely proportional to noise variances. Calculated from the photon transmission rates and applied with pre-calibrated water-based scatter and beam hardening correction [3], the $j^{th}$ projection datum $y_j$ can be written as

$$y_j = h^{-1}\Big(-\log\frac{\lambda_j - \gamma_j}{\lambda_T}\Big). \tag{2}$$

Here $\lambda_T = \int_{\mathcal{E}} \lambda_I(\mathcal{E})\,\mathrm{d}\,\mathcal{E}$ and $\lambda_j = \int_{\mathcal{E}} \lambda_{Rj}(\mathcal{E})\,\mathrm{d}\,\mathcal{E}$ are incident and received photon counts respectively, measured by energy integrating detectors. Incident rates are here assumed constant, but generalization to spatially or temporally varying rates is straightforward. $\gamma_j$ is the estimated scattered photon count, and $h^{-1}()$ represents beam hardening correction. The image $x$ that maximizes (1) embodies the object's attenuation property at a single energy level or effective keV. Metal materials interact with photons of varied energies significantly differently from water's behavior. Thus in metal-affected projections, (2) becomes insufficient to combat X-ray polychromaticity and

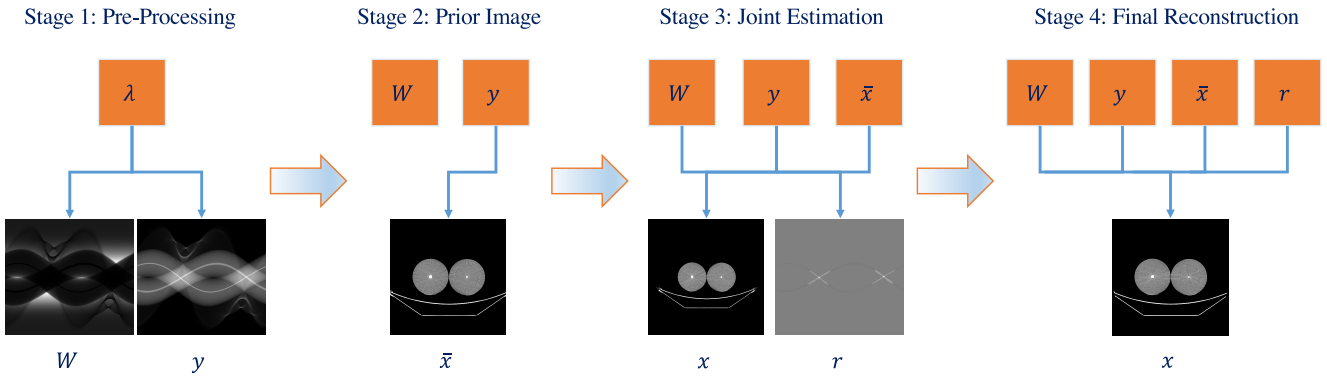


Fig. 2. Flow diagram of the prior-guided MBIR method, starting from raw photon measurements $\lambda$ to the final image $x$ with reduced metal artifacts.

scattering noise. Consequently, the residual biases in $y$, departures from their effective keV values, cause metal artifacts.

Because of the manifold sources leading to the residual biases in the line-integral projections, simple polynomials of $y$, or functions of metal path length, are often inadequately accurate as a model within iterative methods. However, the spatial uniformity of X-ray emission and the nature of scattering mechanisms result in a relatively smooth metal signature within the biased areas. We therefore make the assumption that the residual biases follow a low-pass spatial profile within the metal-affected portions of the sinogram. The least squares problem of (1) is modified to

$$\Psi(x,r) = \frac{1}{2}(y + r - Ax)^T W(y + r - Ax) + U(r), \quad (3)$$

where $r \in R^M$ describes the mismatch between data $y$ and the effective keV line-integrals. The degrees of freedom in $r$ are limited to within metal traces by restricting outside entries to zero. $U(r)$ is a sinogram-domain regularization model to encourage the low-pass feature, given by

$$U(r) = \frac{1}{2}\sum_{(j,m)\in\mathcal{C}} (w_j w_m)^{\frac{1}{2}} s_{j,m}(r_j - r_m)^2. \quad (4)$$

We denote $w_j$ as the $j^{th}$ diagonal element of the statistical data-weighting matrix $W$, and $s_{j,m}$ as the normalized directional coefficients, chosen to be the inverse of the distance to link neighboring projection pairs from the collection $\mathcal{C}$, each of which includes at least one detector within a metal trace. Such a spatially variant scaling is used to regulate data-to-regularization strength, similarly to techniques previously applied in the image domain for spatially homogeneous resolution [41].

To jointly estimate the image $x$ and the bias profile $r$, we propose a prior-guided approach. An image $\bar{x}$ reconstructed using a suitable sinogram completion method serves as both initial condition for reconstruction, and as the "prior" image. Along with $U(r)$, penalizing the distance between x and $\bar{x}$ prevents over-fitting of $r$ in the joint estimation. The objective function is augmented with two additional regularization terms in the image domain:

$$\Phi(x,r) = \Psi(x,r) + R_1(x) + R_2(x;\bar{x}). \quad (5)$$

The first prior $R_1(x)$ describes the edge-tolerant image distribution using a Markov random field (MRF) *a priori* model with spatially adaptive pixel weighting for noise uniformity [42], [43], formulated by

$$R_1(x) = \frac{\beta_1}{2}\sum_{(i,k)\in\mathcal{N}} b_{i,k}\kappa_i\kappa_k\rho(x_i - x_k), \quad (6)$$

and

$$\kappa_i = \left(\sum_{j=1}^{M} w_j A_{ji}^2\right)^{\frac{1}{4}}. \quad (7)$$

The scaling parameter $\beta_1$ is determined by image noise requirements and is adaptive to reconstruction pixel size [44], $b_{i,k}$ are normalized MRF coefficients for neighboring pixel pair collection $\mathcal{N}$ according to inter-voxel distances, and $\kappa_i$ are designed to adapt regularization to data weights and system geometries. The penalty function $\rho()$ is to smooth image texture while preserving edges. Common convex options are exemplified by the log cosh() [45], the generalized Gaussian MRF [46] and Huber-like functions [47]. In this paper, we adopt the $q$-GGMRF model from [44], given by

$$\rho(\Delta) = \frac{|\Delta|^p}{1 + |\Delta/c|^{p-q}}, \quad (8)$$

with $p$ and $q$ set to 2.0 and 1.2, respectively.

The other penalty, $R_2(x;\bar{x})$, is used to regulate large deviation of x from $\bar{x}$ through iterative updates. A simple Gaussian model may be written as

$$R_2(x;\bar{x}) = \frac{\beta_2(n)}{2}(x - \bar{x})^T D(x - \bar{x}). \quad (9)$$

Similarly to $\beta_1$, the scalar $\beta_2$ is also a function of pixel size. The diagonal weighting matrix $D$ augments the spatially variant prior scaling method described in (7) with inclusion of a gradient-based edge preserving term to allow for greater discrepancy near edges. $D$ is composed of entries

$$d_i := \kappa_i^2 \exp\left(-\frac{(\nabla x)_i}{t}\right), \quad (10)$$

with $t$ a constant.

The algorithmic data flow from raw photon measurements $\lambda$ to reconstructed image $x$ is illustrated by the diagram

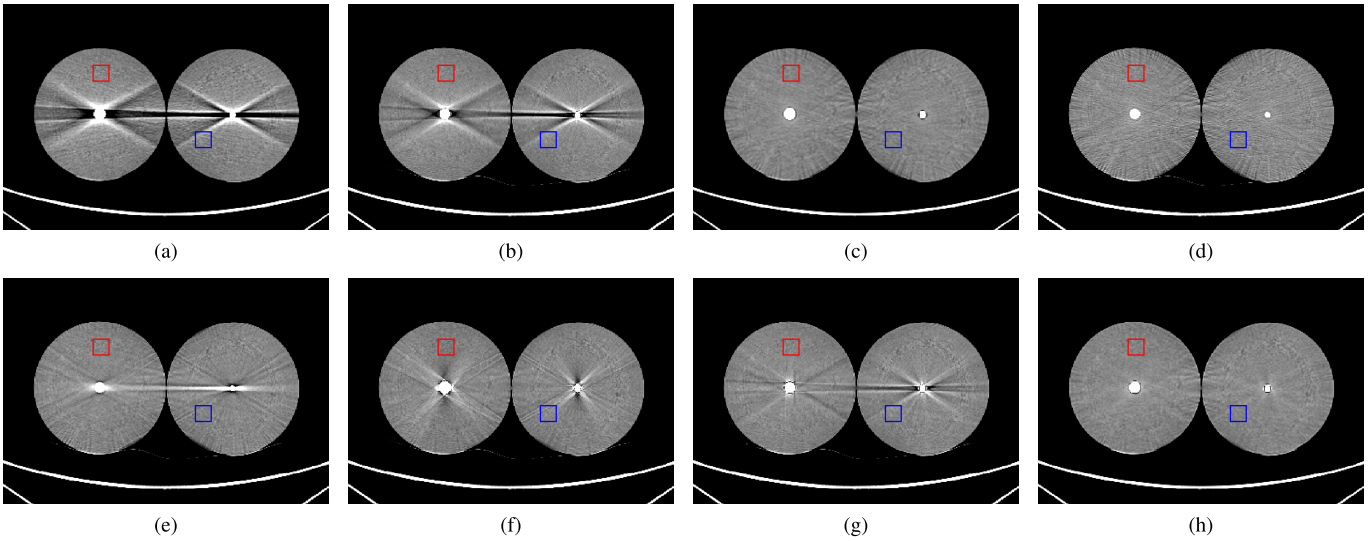


Fig. 3. Center-slice reconstructions of phantom scan data, composed of two water cylinders with metal inserts. (a): FBP; (b): MBIR with standard water-corrected sinogram data; (c): NMAR, a state-of-the-art sinogram completion method; (d): Least squares IR with NMAR-modified sinogram, post-processed by superposing metals in image domain; (e): MBIR with NMAR-modified sinogram, post-processed by superposing metals in image domain; (f): MBIR with data replacement in metal traces by forward projection of the NMAR image; (g): Joint estimation of image and sinogram bias without $R_2(x;\bar{x})$ penalty term; (h): proposed algorithm using NMAR to guide sinogram correction. Display window [−100, 100] HU. Two ROI's, R1 in red and R2 in blue, are selected for quantitative evaluation.

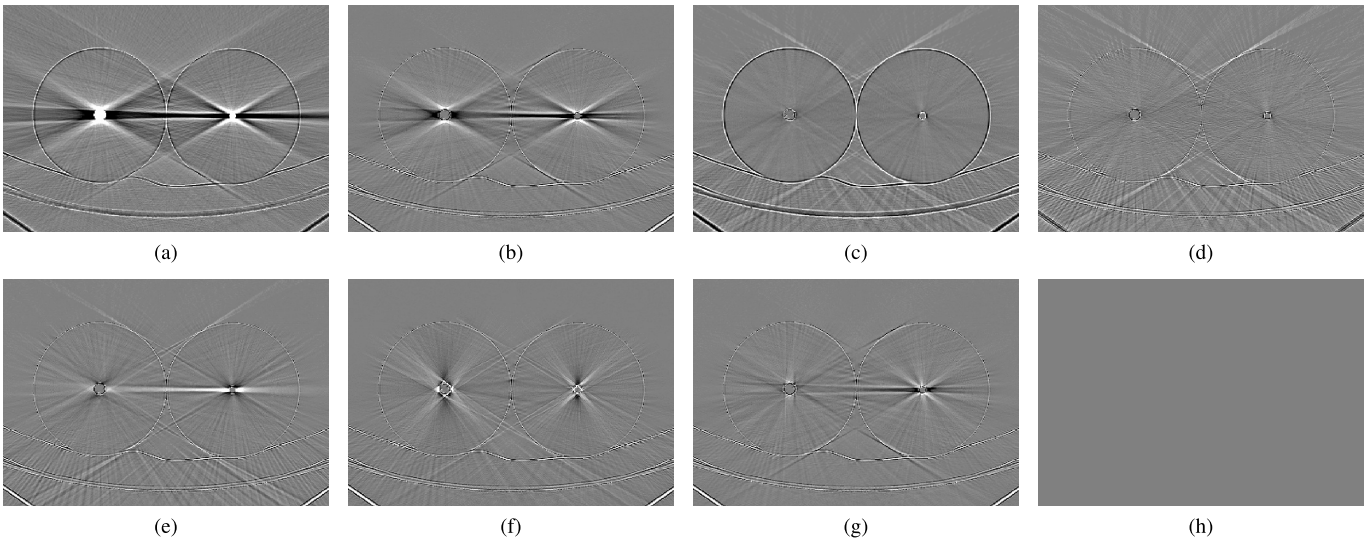


Fig. 4. Center-slice difference images of phantom reconstructions, using proposed method as reference. (a): FBP; (b): MBIR with standard water-corrected sinogram data; (c): NMAR; (d): Least squares IR with NMAR-modified sinogram, post-processed by superposing metals in image domain; (e): MBIR with NMAR-modified sinogram, post-processed by superposing metals in image domain; (f): MBIR with data replacement in metal traces by forward projection of the NMAR image; (g): Joint estimation of image and sinogram bias without $R_2(x;\bar{x})$ penalty term; (h): proposed algorithm using NMAR to guide sinogram correction. Display window [−100, 100] HU.

in Fig. 2. During the pre-processing stage, line-integral projections with corresponding statistical weights are computed [40], and water-based scatter and beam hardening corrections are applied. The prior image $\bar{x}$ is then computed from $y$ using the NMAR sinogram completion approach, followed by filtered back-projection (FBP). $\bar{x}$ also serves as initial condition in the iterative image reconstruction process. In stage 3, the image $x$ and the residual sinogram bias $r$ are jointly estimated by alternating minimization of the objective function in (5).

$$x^{(n)} = \arg\min_{x} \Phi(x^{(n-1)}, r^{(n-1)}), \tag{11}$$

$$r^{(n)} = \arg\min_{r} \Phi(x^{(n)}, r^{(n-1)}). \tag{12}$$

The optimization problem can be solved using surrogates algorithms [48]–[50].

As the solution of the joint estimation problem converges in Stage 3, the estimate of $r$ reaches a smooth compensation for data inconsistencies that is compatible with the relatively artifact-free NMAR image due to the prior image penalty. In Stage 4, the strength of the prior image penalty is decreased in order that the final estimate can evolve toward the noise and resolution enhancements typical of MBIR. We continue with an image refinement step by fixing $r$ and reconstructing $x$ with reduced weighting on $R_2(x;\bar{x})$ penalty. To indicate the dependence among image iterations in stage 3 and stage 4, we augment the $\beta_2$ dependence with the iteration index $n$.

TABLE I
MEAN AND STANDARD DEVIATION MEASUREMENTS (HU) AT SELECTED ROI'S OF IMAGES IN FIGURE 3

| ROI | FBP | MBIR | NMAR | 3 (d) | 3 (e) | 3 (f) | 3 (g) | Proposed |
|---|---|---|---|---|---|---|---|---|
| R1 Mean | 5.0 | 4.3 | 3.3 | 6.5 | 4.1 | -4.0 | 4.9 | 2.8 |
| Std. Dev. | 9.6 | 9.2 | 6.8 | 10.2 | 9.2 | 8.8 | 8.9 | 6.9 |
| R2 Mean | 8.9 | 10.0 | 1.3 | 3.9 | 2.7 | 7.3 | 7.4 | 3.4 |
| Std. Dev. | 17.6 | 11.2 | 6.6 | 13.1 | 8.8 | 11.6 | 9.6 | 6.7 |

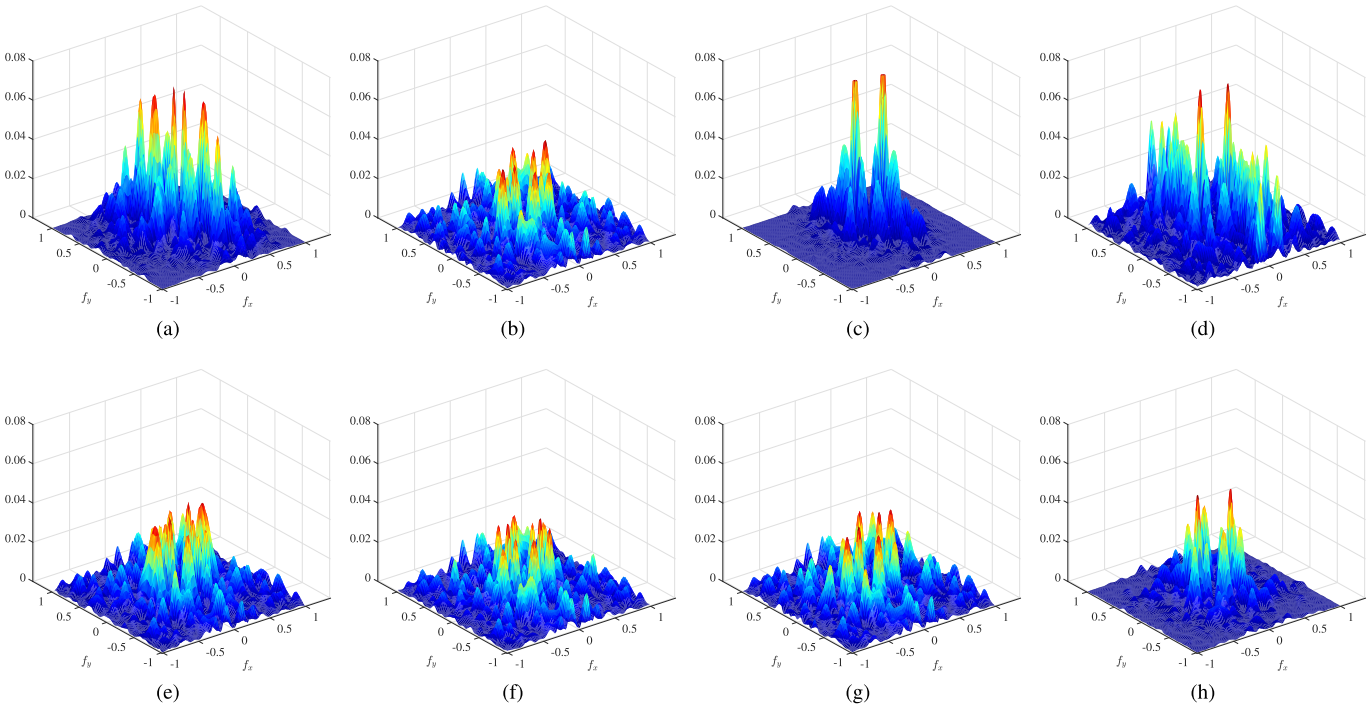


Fig. 5. Welch-type periodogram noise power spectral density estimates in corresponding images of Fig. 3 at ROI R1. (a): FBP; (b): MBIR with standard water-corrected sinogram data; (c): NMAR; (d): Least squares IR with NMAR-modified sinogram, post-processed by superposing metals in image domain; (e): MBIR with NMAR-modified sinogram, post-processed by superposing metals in image domain; (f): MBIR with data replacement in metal traces by forward projection of the NMAR image; (g): Joint estimation of image and sinogram bias without $R_2(x; \bar{x})$ penalty term; (h): proposed algorithm using NMAR to guide sinogram correction.

## III. RESULTS AND DISCUSSION

We applied the proposed algorithm on cone-beam CT scan data acquired on a Discovery CT750 HD scanner (GE Healthcare, Waukesha, WI). All data were composed of 984 views per rotation, with a detector array made up of 888 × 64 subdetectors, having maximum collimation of 40 mm at isocenter. Subsequently, NMAR results were computed based on [14]; conventional MBIR results were achieved by applying the algorithm in [42] and [44] and a gradient-based iterative reconstruction (IR) approach for optimization [49], [50] of the objective function

$$\varphi(x) = \frac{1}{2}(y - Ax)^T W(y - Ax) + R_1(x). \qquad (13)$$

Resolutions of reconstructed images were 512 × 512 pixels, with slice thickness of 0.625 mm. All MBIR results were obtained after 10 iterations with the channelized preconditioner in [50] to dramatically accelerate convergence, beyond which we have found empirically negligible change in the results. The proposed method also finished with 10 image updates, equally divided into stage 3 and stage 4. In stage 3, the scaling parameters $\beta_1$ and $\beta_2(n)$ $(n = 1, 2, \ldots, 5)$ were set to an experimentally chosen, identical value of $\beta_1$ in optimizing (13) from [44]. In stage 4, $\beta_2(n)$ $(n = 6, 7, \ldots, 10)$ was reduced to one-tenth of the value of $\beta_1$. The parameter $c$ in (8) and $t$ in (10) were fixed at 20 HU.

Addition of the NMAR prior to the MBIR reconstruction comes at a relatively modest computational cost. In a typical example below, simple MBIR required 18 minutes, 44 seconds, while the prior-guided MBIR version required 20 minutes, 35 seconds, a penalty of under 10%. Computation of the precise forward model dominates the time. All MBIR reconstructions implemented distance-driven projection [51]. The algorithm was not optimized to hardware of Intel Xeon E5-2620 v4 CPU, however, and this comparison should not be considered precise.

We first applied the prior-guided iterative MAR algorithm on axial phantom scan data at 120 kVp, 640 mA

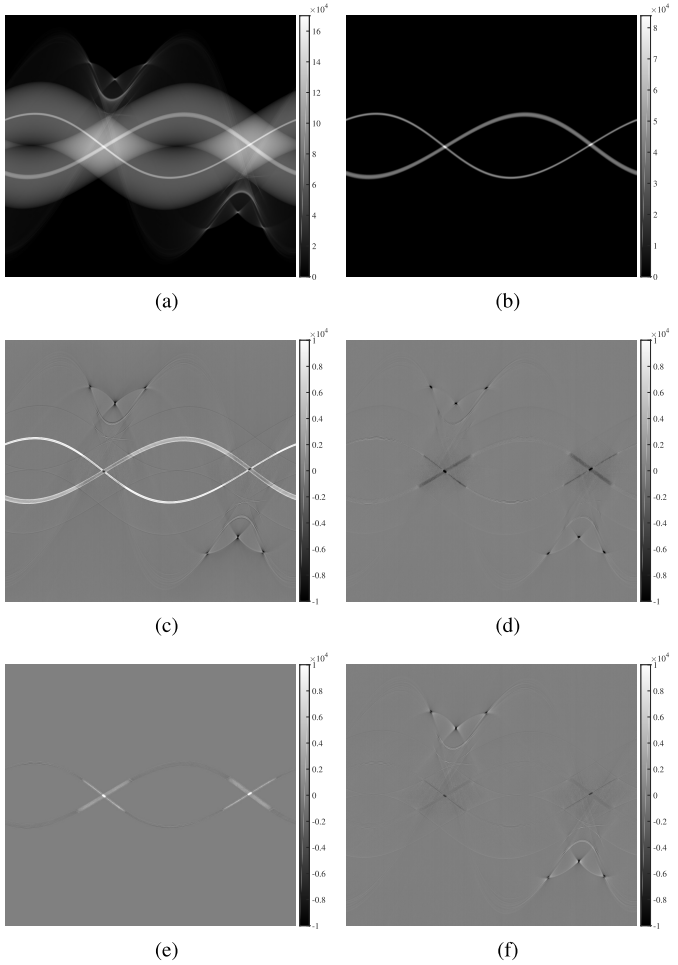


Fig. 6. Sinogram domain analysis from center row of the detector array, corresponding to the slice location of Fig. 3. (a): Water-corrected projection measurements $y$ from data pre-processing stage; (b): Metal trace by forward projection of thresholded metal inserts; (c): initial error sinogram $y - Ax^{(0)}$; (d): converged error sinogram ($y - Ax$) using standard MBIR algorithm in (13); (e): estimated projection bias profile $r$ using proposed approach; (f): converged error sinogram ($y + r - Ax$) using proposed approach in (5).

and 1 sec/rotation. Two water phantoms with diameter of 125 mm were placed side-by-side, supplemented with a 9.5 mm titanium rod in one and a 4.8 mm stainless steel rod in the other. The reconstruction FOV is 400 mm, and pixel size is 0.78 mm. As shown in Figs. 3 (a) and (b), the FBP and MBIR results from water-corrected data suffer from artifacts caused by metals. The heaviest biases appear as a dark streak along the line connecting the two rods, accompanied by bright sharp edges on each side. Additionally, each rod creates abrupt transitions in line-integral densities as it interacts with the boundaries of the other cylinder, leading to cross-shaped artifacts in the middle of each cylinder, formed with bright and dark shades. Thanks to the statistical data weighting and the *a priori* regularization used in objective function (13), Fig. 3 (b) contains lighter biases than does Fig. 3 (a).

The NMAR image presented in Fig. 3 (c) has the streaking and shading artifacts largely removed. However, the radially-oriented texture in the cylinders suggests imperfection in data replacement that compromises image quality, particularly in

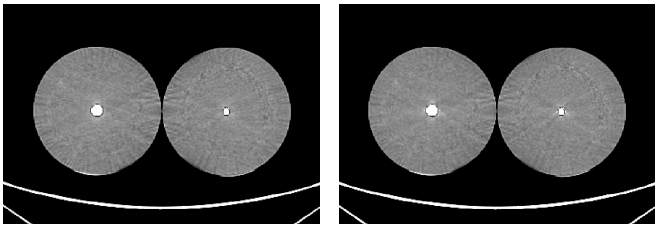


Fig. 7. Additional center-slice reconstructions of the phantom data, with different $\beta_2$ values in stage 4 reconstruction. (a): $\beta_2$ as half of the value used in Fig. 3 (h); (b): $\beta_2$ as twice of the value used in Fig. 3 (h); Display window [−100, 100] HU.

the regions where metal artifacts were not present initially. Fig. 3 (d) uses the same inpainted sinogram from the NMAR technique for least squares iterative reconstruction, which optimizes objective function similar to (13) but with $W$ as the identity matrix. Similarly to NMAR, the result, with metals added in post-processing, suffers from the radially-oriented artifacts.

Fig. 3 (e), however, attempts to reconstruct the NMAR-modified sinogram with MBIR in (13). Metal artifacts are reduced in comparison to Fig. 3 (b), but some artifacts appear in reversed shades, particularly along the horizontal line connecting two rods. Near the cylinder boundaries, the high-frequency error patterns resemble the ones in Fig. 3 (c). In the mode of performing MBIR on linearized projections, Fig. 3 (f) was obtained by replacing projection data in metal traces with forward projection of the NMAR image. While suffering from correlated artifact patterns, the image was also impacted by limitations of HU accuracy in NMAR, especially along metal edges. The weighting of data inverse to approximate variance in MBIR is key to its image quality improvements in cases where the entire system is accurately modeled. However, under modeling errors, artifacts may be exacerbated compared to uniform weighting, in a manner which is not easily predicted.

The image shown in Fig. 3 (g) is reconstructed similarly to the proposed method but in the absence of $R_2(x; \bar{x})$ penalty term. It suggests that without penalizing of pixel value's departure from initial condition or prior image, the image estimate $x$ and sinogram bias esimtate $r$ would compete for compensating the mismatch between $y$ and $Ax$. Thus comes the result with reduced artifacts but still compromised overall quality. Fig. 3 (h), reconstructed by the proposed algorithm, is more nearly free of prominent metal artifacts. Though the error variance is similar to that of NMAR, the noise texture in the water substance is more uniform and less spatially correlated than in the NMAR image. Particularly in the top and bottom regions of the water cylinders where image quality was less affected by the metals, the proposed approach was able to retain most of the MBIR-type noise characteristics.

Local means and standard deviations in constant-valued regions are compared in Table I. We see that our proposed method does not consistently exhibit the lowest noise power of the methods presented. However, in this work we seek as first priority metal artifact suppression, accompanied by noise control and overall resolution competitive with

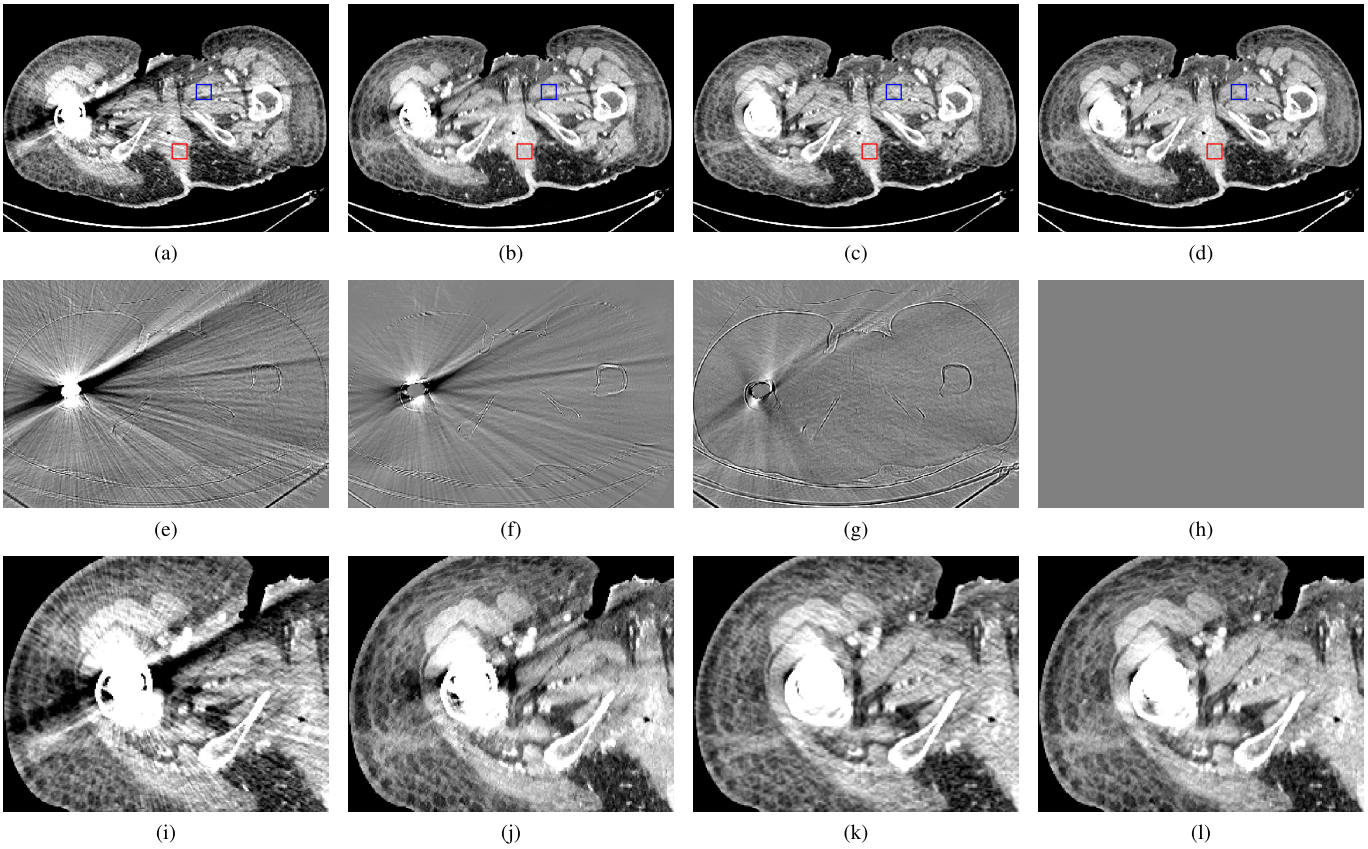


Fig. 8. Clinical scan data with metal hip implant of slice 16 in reconstructed volume. (a): FBP; (b): MBIR with standard water-corrected sinogram data; (c): NMAR; (d): proposed NMAR-guided MBIR algorithm. Middle row are difference images using proposed method as reference. Bottom row images are corresponding locally zoomed-in presentations of the top row results near the metal joint. Display window [−100, 100] HU. Two ROI's, R3 in red and R4 in blue, are selected for quantitative evaluation.

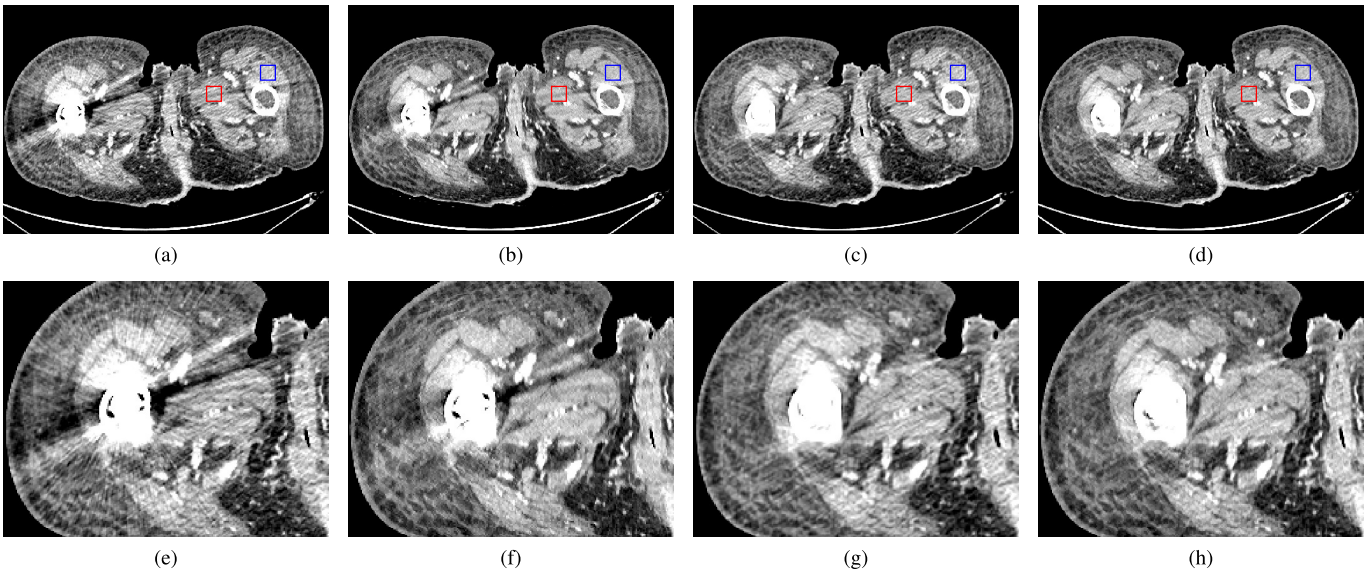


Fig. 9. Clinical scan data with metal hip implant of slice 32 in reconstructed volume. (a): FBP; (b): MBIR with standard water-corrected sinogram data; (c): NMAR; (d): proposed NMAR-guided MBIR algorithm. Bottom row images are corresponding locally zoomed-in presentations of the top row results near the metal joint. Display window [−100, 100] HU. Two ROI's, R5 in red and R6 in blue, are selected for quantitative evaluation.

conventional MBIR. As a more complete comparison of phantom reconstruction errors away from major artifact areas, noise power spectra of a selected homogeneous ROI are plotted in Fig. 5. The two relatively prominent spectral peaks in Fig.5 (c) correspond to the oriented error described earlier in the NMAR image. Fig. 5 (h) is the local spectrum of

the reconstruction errror with the proposed method, with somewhat less concentrated spectral power than the NMAR result. The broader-spectrum error in Fig. 5 (b) is more typical of noise from an unprocessed sinogram.

The structural guidance provided by the NMAR image stabilizes estimation of the sinogram bias $r$. As a result, the profile of $r$ transitions smoothly across detector channels and view angles within the metal trace. In Fig. 6, illustration in the sinogram domain is provided. At the beginning, the error sinogram between measured data and forward projection of NMAR shows significant gaps, particularly near the metal traces, shown in Fig. 6 (c). This is mainly caused by the reconstruction separation of metal and non-metal materials in sinogram completion methods. Without any compensation for the metal-affected projections, the converged error sinogram shows significant, correlated discrepancies between data and the forward projections, as shown in Fig. 6 (d). Notice that the two sets of triple dark points correspond to three of the CT table edges. Those biases have little effect on the reconstruction in the region of interest. In stage 3 of the proposed algorithm, the bias $r$ profile is estimated, shown in Fig. 6 (e). Qualitatively, the profile looks like the complement to the error sinogram in Fig. 6 (d). With the corrected projection estimation $(y + r)$, the converged error sinogram appears substantially flatter across the views. Fig. 6 (f) shows that the jointly estimated projection bias removed the consequential data inconsistencies.

In Stage 4 of the proposed algorithm, we decrease $\beta_2$ by a factor of 10 from its value in the joint estimation stage. In practice, the result is not highly sensitive to the choice of the final $\beta_2$, as illustrated by Fig. 7, suggesting that structured data inconsistencies have been effectively removed in Stage 3.

The proposed prior-guided MBIR algorithm was also applied on a clinical torso scan, where a metal hip joint replacement present in the femur caused shading artifacts across the image volume. The data were acquired with tube settings of 120 kVp, 750 mA and speed of 0.5 sec/rotation in helical mode of pitch ratio 63/64. Reconstructed images at two slice locations 10 mm apart are presented in Figs. 8 and 9 respectively, in an effort to demonstrate image quality consistency across the reconstructed volume. Each has an FOV of 400 mm and pixel size of 0.78 mm. As shown in Figs. 8 (a) and 9 (a), the in-plane FBP images suffer from major metal artifacts. Streaks and shadings heavily degrade the diagnostic quality by corrupting the nearby soft tissue and bone values. In comparison, standard MBIR results are shown in Figs. 8 (b) and 9 (b), which contain similarly structured artifacts as FBP's but with substantially reduced magnitude, thanks to the statistical weighting and *a priori* image model. The NMAR images in Figs. 8 (c) and 9 (c) show removal of prominent artifacts. There are some remaining shadings around the metal and high-frequency noise patterns in soft tissues. In Figs. 8 (d) and 9 (d), the proposed MAR approach combines the merits of MBIR and NMAR, resulting in reduced metal artifacts as well as improved image texture and noise control. Tables II and III show the combined method holds local variances to the levels of conventional MBIR.

TABLE II
MEAN AND STANDARD DEVIATION MEASUREMENTS (HU) AT SELECTED ROI'S OF IMAGES IN FIGURE 8

| ROI | FBP | MBIR | NMAR | Proposed |
|---|---|---|---|---|
| R3 Mean | 56.1 | 61.0 | 57.0 | 57.1 |
| Std. Dev. | 22.4 | 11.5 | 14.9 | 11.3 |
| R4 Mean | 41.7 | 38.2 | 43.0 | 36.4 |
| Std. Dev. | 30.9 | 23.6 | 20.1 | 17.3 |

TABLE III
MEAN AND STANDARD DEVIATION MEASUREMENTS (HU) AT SELECTED ROI'S OF IMAGES IN FIGURE 9

| ROI | FBP | MBIR | NMAR | Proposed |
|---|---|---|---|---|
| R5 Mean | 40.6 | 44.0 | 42.2 | 38.6 |
| Std. Dev. | 24.6 | 17.0 | 20.2 | 17.2 |
| R6 Mean | 54.9 | 50.4 | 53.6 | 48.4 |
| Std. Dev. | 20.0 | 15.7 | 18.9 | 16.3 |

TABLE IV
MEAN AND STANDARD DEVIATION MEASUREMENTS (HU) AT SELECTED ROI'S OF IMAGES IN FIGURE 10

| ROI | FBP | MBIR | NMAR | Proposed |
|---|---|---|---|---|
| R7 Mean | 98.4 | 104.0 | 97.5 | 82.5 |
| Std. Dev. | 44.7 | 37.5 | 19.1 | 12.3 |
| R8 Mean | 65.8 | 83.5 | 88.9 | 75.0 |
| Std. Dev. | 17.3 | 27.2 | 12.0 | 10.0 |

TABLE V
MEAN AND STANDARD DEVIATION MEASUREMENTS (HU) AT SELECTED ROI'S OF IMAGES IN FIGURE 11

| ROI | FBP | MBIR | NMAR | Proposed |
|---|---|---|---|---|
| R9 Mean | 76.3 | 70.5 | 85.9 | 61.8 |
| Std. Dev. | 59.1 | 58.7 | 17.1 | 12.4 |
| R10 Mean | 83.4 | 78.4 | 32.2 | 58.2 |
| Std. Dev. | 25.4 | 34.5 | 15.1 | 11.7 |

Finally, we applied the proposed algorithm on two sets of dental exams. They were both scanned at 120 kVp. 750 mA, with speed of 0.5 sec/rotation in axial mode. Both reconstruction FOV's were 240 mm with pixel size of 0.49 mm. One of the exams contains one dental filling, as shown in Fig. 10; the other contains two fillings in Fig. 11. Dental fillings are made from various materials and are often irregularly shaped and relatively small in size. Additionally, teeth themselves are composed of high-density elements. Reduction of artifacts caused by dental fillings is widely considered among the most challenging metal scenarios. As shown in Figs. 10 and 11, the FBP and MBIR images are corrupted by heavy streaking artifacts, originating from the metals and extending through the transaxial plane. The NMAR algorithm is effective in mitigating the artifacts, but residual shadings are still noticeable. Particularly in the case of two fillings, the image in Fig. 11 (c) fails to recover uniform soft tissue

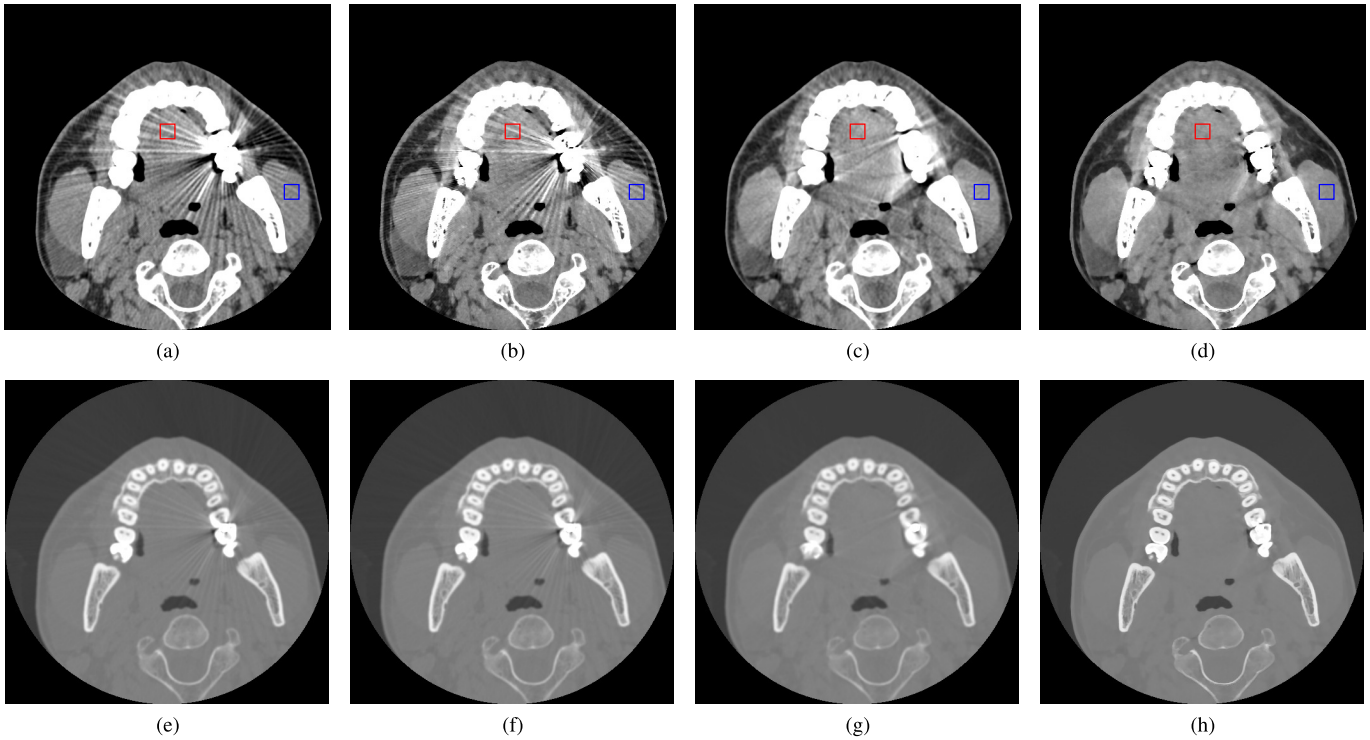

Fig. 10. Reconstruction of clinical dental scan data with a single metal filling. (a): FBP; (b): MBIR with standard water-corrected sinogram data; (c): NMAR; (d): proposed NMAR-guided MBIR algorithm. Display window [−200, 200] HU. Bottom row images from (e) - (h) are corresponding wide-window displacement of the top row results with window width of 4000 HU. Two ROI's, R7 in red and R8 in blue, are selected for quantitative evaluation.

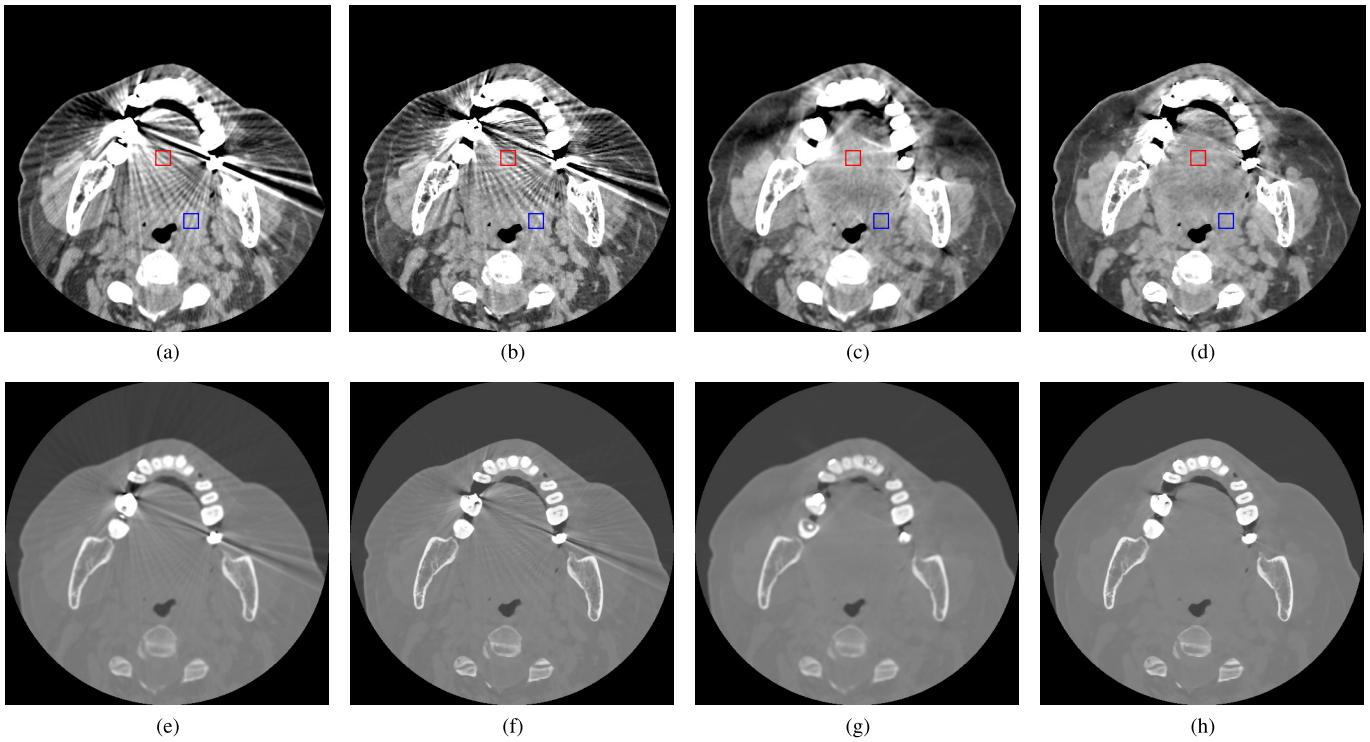

Fig. 11. Reconstruction of clinical dental scan data with two metal fillings. (a): FBP; (b): MBIR with standard water-corrected sinogram data; (c): NMAR; (d): proposed NMAR-guided MBIR algorithm. Display window [−200, 200] HU. Bottom row images from (e) - (h) are corresponding wide-window displacement of the top row results with window width of 4000 HU. Two ROI's, R9 in red and R10 in blue, are selected for quantitative evaluation.

around the teeth area. With the wide display window, shown in Fig. 11 (g), the shapes and densities of the teeth are not well retained compared to FBP or MBIR results. The proposed prior-guided approach produces significantly cleaner and more consistent artifact reduction across the images. The tissue textures remain on the same level as the non-metal-affected

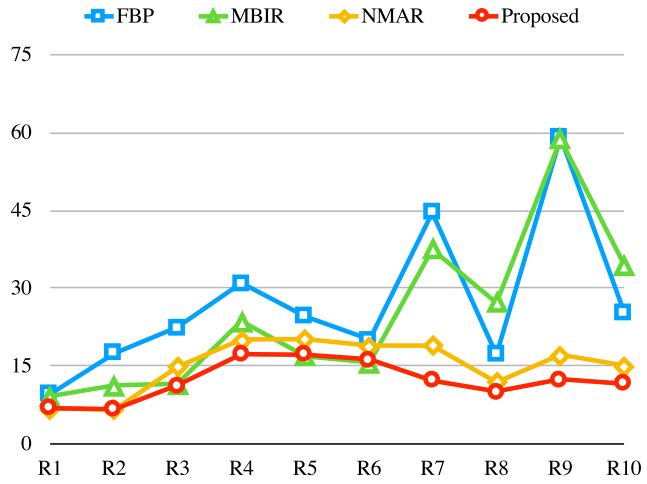


Fig. 12. Plot of standard deviations of 10 ROIs across exams.

regions in standard MBIR. The bone and tooth details are sharply displayed in the wide window images.

To evaluate the overall performance of the proposed MAR solution, standard deviation measurements from Table I to Table V are plotted in Fig. 12. Across all 10 selected ROI's, the proposed method managed to suppress noise in uniform regions while preserving high-frequency information, such as bone edges and teeth shapes.

## IV. Conclusion

We proposed a prior-based iterative solution to reduce high-attenuation materials (e.g., metal) induced artifacts. Preliminary phantom and clinical results show great promise. The algorithm takes an analytical reconstruction from sinogram completion-based MAR approaches as a "prior" image, and guides the iterative estimation of the nonlinear biases in the projection measurements. In this paper, we applied our approach with the well-known sinogram completion method NMAR, and showed appreciable improvements compared to either MBIR or NMAR alone, or conventional MBIR with corrected data as input. This framework can be further optimized to incorporate the full merits of iterative reconstruction with more recent advances in analytical sinogram completion MAR techniques

Strictly speaking, the prior-guided approach to joint estimate $x$ and $r$ as in (5) is a form of sinogram completion method, in the sense that the metal-caused nonlinear projection biases are not systematically corrected using information about the X-ray spectrum or metal materials. Taking the analytical construction result $\bar{x}$ as additional knowledge, we estimate the biases by optimizing an objective function in (5). With this supplemental information incorporated into statistical reconstruction, we are able to achieve smooth and consistent correction in sinogram domain, which translates to superior image quality in spatial domain compared to conventional sinogram completion methods.

Reconstructed by FBP, the sinogram completion methods, such as NMAR, are generally efficient to compute compared to iterative reconstruction. Therefore, the prior-based reconstruction algorithm outperforms standard MBIR with metal present at relatively little added cost.

## References

[1] R. A. Brooks and G. Di Chiro, "Beam hardening in X-ray reconstructive tomography," *Phys. Med. Biol.*, vol. 21, no. 3, p. 390, 1976.
[2] L. M. Zatz and R. E. Alvarez, "An inaccuracy in computed tomography: The energy dependence of CT values," *Radiology*, vol. 124, no. 1, pp. 91–97, 1977.
[3] J. Hsieh, *Computed Tomography: Principles, Design, Artifacts, and New Developments*, 2nd ed. Bellingham, WA, USA: SPIE, 2009.
[4] W. D. McDavid, R. G. Waggener, W. H. Payne, and M. J. Dennis, "Correction for spectral artifacts in cross-sectional reconstruction from X rays," *Med. Phys.*, vol. 4, no. 1, pp. 54–57, 1977.
[5] G. T. Herman, "Correction for beam hardening in computed tomography," *Phys. Med. Biol.*, vol. 24, no. 1, p. 81, 1979.
[6] O. Klein and Y. Nishina, "Über die streuung von strahlung durch freie elektronen nach der neuen relativistischen quantendynamik von dirac," *Zeitschrift Physik*, vol. 52, nos. 11–12, pp. 853–868, 1929.
[7] N. Haramati *et al.*, "CT scans through metal scanning technique versus hardware composition," *Comput. Med. Imag. Graph.*, vol. 18, no. 6, pp. 429–434, Nov./Dec. 1994.
[8] D. D. Robertson, P. J. Weiss, E. K. Fishman, D. Magid, and P. S. Walker, "Evaluation of CT techniques for reducing artifacts in the presence of metallic orthopedic implants," *J. Comput. Assist. Tomogr.*, vol. 12, no. 2, pp. 236–241, Mar. 1988.
[9] J. A. Veiga-Pires and M. Kaiser, "Artefacts in CT scanning," *Brit. J. Radiol.*, vol. 52, no. 614, pp. 156–157, 1979.
[10] W. A. Kalender, R. Hebel, and J. Ebersberger, "Reduction of CT artifacts caused by metallic implants," *Radiology*, vol. 164, pp. 576–577, Aug. 1987.
[11] G. H. Glover and N. J. Pelc, "An algorithm for the reduction of metal clip artifacts in CT reconstructions," *Med. Phys.*, vol. 8, no. 6, pp. 799–807, 1981.
[12] H. K. Tuy, "A post-processing algorithm to reduce metallic clip artifacts in CT images," *Eur. Radiol.*, vol. 3, no. 2, pp. 129–134, Apr. 1993.
[13] M. Kachelrieb and W. A. Kalender, "Improving PET/CT attenuation correction with iterative CT beam hardening correction," in *Proc. IEEE Nucl. Sci. Symp. Conf. Rec.*, vol. 4, Oct. 2005, p. 5.
[14] E. Meyer, R. Raupach, M. Lell, B. Schmidt, and M. Kachelrie, "Normalized metal artifact reduction (NMAR) in computed tomography," *Med. Phys.*, vol. 37, no. 10, pp. 5482–5493, 2010.
[15] E. Meyer, C. Maaß, M. Baer, R. Raupach, B. Schmidt, and M. Kachelrieß, "Empirical scatter correction (ESC): A new CT scatter correction method and its application to metal artifact reduction," in *Proc. IEEE Nucl. Sci. Symp. Med. Imag. Conf.*, Oct./Nov. 2010, pp. 2036–2041.
[16] T. Heußer, M. Brehm, L. Ritschl, S. Sawall, and M. Kachelrieß, "Prior-based artifact correction (PBAC) in computed tomography," *Med. Phys.*, vol. 41, no. 2, p. 021906, 2014.
[17] R. L. Morin and D. E. Raeside, "A pattern recognition method for the removal of streaking artifact in computed tomography," *Radiology*, vol. 141, no. 1, pp. 229–233, Oct. 1981.
[18] S. Singh, K. Muralidhar, and P. Munshi, "Image reconstruction from incomplete projection data using combined ART-CBP algorithm," *Defence Sci. J.*, vol. 52, no. 3, pp. 303–316, 2002.
[19] E. Meyer, R. Raupach, M. Lell, B. Schmidt, and M. Kachelrieß, "Frequency split metal artifact reduction (FSMAR) in computed tomography," *Med. Phys.*, vol. 39, no. 4, pp. 1904–1916, 2012.
[20] D. Pal, K. S. Sharma, and J. Hsieh, "Metal artifact correction algorithm for CT," in *Proc. IEEE Nucl. Sci. Symp. Med. Imag. Conf. (NSS/MIC)*, Oct./Nov. 2013, pp. 1–4.
[21] P. M. Joseph and R. D. Spital, "A method for correcting bone induced artifacts in computed tomography scanners," *J. Comput. Assist. Tomogr.*, vol. 2, no. 1, pp. 100–108, 1978.
[22] P. M. Joseph and C. Ruth, "A method for simultaneous correction of spectrum hardening artifacts in CT images containing both bone and iodine," *Med. Phys.*, vol. 24, no. 10, pp. 1629–1634, 1997.
[23] J. Hsieh, R. C. Molthen, C. A. Dawson, and R. H. Johnson, "An iterative approach to the beam hardening correction in cone beam CT," *Med. Phys.*, vol. 27, no. 1, pp. 23–29, 2000.
[24] P. J. La Rivière, J. Bian, and P. A. Vargas, "Penalized-likelihood sinogram restoration for computed tomography," *IEEE Trans. Med. Imag.*, vol. 25, no. 8, pp. 1022–1036, Aug. 2006.

[25] B. E. Oppenheim, "Reconstruction tomography from incomplete projections," Univ. Chicago, Dept. Radiol., Franklin McLean Memorial Res. Inst., Chicago, IL, USA, Tech. Rep. CONF-750465-2, 1975.

[26] G. Wang, D. L. Snyder, J. A. O'Sullivan, and M. W. Vannier, "Iterative deblurring for CT metal artifact reduction," *IEEE Trans. Med. Imag.*, vol. 15, no. 5, pp. 657–664, Oct. 1996.

[27] B. De Man, J. Nuyts, P. Dupont, G. Marchal, and P. Suetens, "Reduction of metal streak artifacts in X-ray computed tomography using a transmission maximum *a posteriori* algorithm," *IEEE Trans. Nucl. Sci.*, vol. 47, no. 3, pp. 977–981, Jun. 2000.

[28] K. Kuya, Y. Shinohara, A. Kato, M. Sakamoto, M. Kurosaki, and T. Ogawa, "Reduction of metal artifacts due to dental hardware in computed tomography angiography: Assessment of the utility of model-based iterative reconstruction," *Neuroradiology*, vol. 59, no. 3, pp. 231–235, 2017.

[29] C. Lemmens, D. Faul, and J. Nuyts, "Suppression of metal artifacts in CT using a reconstruction procedure that combines MAP and projection completion," *IEEE Trans. Med. Imag.*, vol. 28, no. 2, pp. 250–260, Feb. 2009.

[30] P. Jin, D. H. Ye, and C. A. Bouman, "Joint metal artifact reduction and segmentation of CT images using dictionary-based image prior and continuous-relaxed potts model," in *Proc. IEEE Int. Conf. Image Process. (ICIP)*, Sep. 2015, pp. 798–802.

[31] P. Jin, C. A. Bouman, and K. D. Sauer, "A model-based image reconstruction algorithm with simultaneous beam hardening correction for X-ray CT," *IEEE Trans. Comput. Imag.*, vol. 1, no. 3, pp. 200–216, Sep. 2015.

[32] J. W. Stayman, Y. Otake, J. L. Prince, A. J. Khanna, and J. H. Siewerdsen, "Model-based tomographic reconstruction of objects containing known components," *IEEE Trans. Med. Imag.*, vol. 31, no. 10, pp. 1837–1848, Oct. 2012.

[33] V. Ruth, D. Kolditz, C. Steiding, and W. A. Kalender, "Metal artifact reduction in X-ray computed tomography using computer-aided design data of implants as prior information," *Investigative Radiol.*, vol. 52, no. 6, pp. 349–359, 2017.

[34] B. D. Man, J. Nuyts, P. Dupont, G. Marchal, and P. Suetens, "An iterative maximum-likelihood polychromatic algorithm for CT," *IEEE Trans. Med. Imag.*, vol. 20, no. 10, pp. 999–1008, Oct. 2001.

[35] K. Van Slambrouck and J. Nuyts, "Metal artifact reduction in computed tomography using local models in an image block-iterative scheme," *Med. Phys.*, vol. 39, no. 11, pp. 7080–7093, 2012.

[36] I. A. Elbakri and J. A. Fessler, "Statistical image reconstruction for polyenergetic X-ray computed tomography," *IEEE Trans. Med. Imag.*, vol. 21, no. 2, pp. 89–99, Feb. 2002.

[37] S. Srivastava and J. A. Fessler, "Simplified statistical image reconstruction for polyenergetic X-ray CT," in *Proc. IEEE Nucl. Sci. Symp.*, Oct. 2005, pp. 1551–1555. [Online]. Available: https://ieeexplore.ieee.org/document/1596614

[38] M. Abella and J. A. Fessler, "A new statistical image reconstruction algorithm for polyenergetic X-ray CT," in *Proc. IEEE Int. Symp. Biomed. Imag., Nano Macro (ISBI)*, Jun./Jul. 2009, pp. 165–168.

[39] K. Sauer and C. Bouman, "A local update strategy for iterative reconstruction from projections," *IEEE Trans. Signal Process.*, vol. 41, no. 2, pp. 534–548, Feb. 1993.

[40] Z. Chang *et al.*, "Modeling and pre-treatment of photon-starved CT data for iterative reconstruction," *IEEE Trans. Med. Imag.*, vol. 36, no. 1, pp. 277–287, Jan. 2017.

[41] J. A. Fessler and W. L. Rogers, "Spatial resolution properties of penalized-likelihood image reconstruction: Space-invariant tomographs," *IEEE Trans. Image Process.*, vol. 5, no. 9, pp. 1346–1358, Sep. 1996.

[42] Z. Chang *et al.*, "Adaptive regularization for uniform noise covariance in iterative 3D CT," in *Proc. 13th Int. Meeting Fully Three-Dimensional Image Reconstruction Radiol. Nucl. Med.*, Newport, RI, USA, May/Jun. 2015, pp. 256–259.

[43] J. H. Cho and J. A. Fessler, "Regularization designs for uniform spatial resolution and noise properties in statistical image reconstruction for 3-D X-ray CT," *IEEE Trans. Med. Imag.*, vol. 34, no. 2, pp. 678–689, Feb. 2015.

[44] J.-B. Thibault, K. D. Sauer, C. A. Bouman, and J. Hsieh, "A three-dimensional statistical approach to improved image quality for multislice helical CT," *Med. Phys.*, vol. 34, no. 11, pp. 4526–4544, Nov. 2007.

[45] P. J. Green, "Bayesian reconstructions from emission tomography data using a modified EM algorithm," *IEEE Trans. Med. Imag.*, vol. 9, no. 1, pp. 84–93, Mar. 1990.

[46] C. Bouman and K. Sauer, "A generalized Gaussian image model for edge-preserving MAP estimation," *IEEE Trans. Image Process.*, vol. 2, no. 3, pp. 296–310, Jul. 1993.

[47] R. Stevenson and E. Delp, "Fitting curves with discontinuities," in *Proc. 1st Int. Workshop Robust Comput. Vis.*, Oct. 1990, pp. 127–136.

[48] J. A. Fessler and H. Erdogan, "A paraboloidal surrogates algorithm for convergent penalized-likelihood emission image reconstruction," in *Proc. IEEE Nucl. Sci. Symp., Conf. Rec.*, vol. 2, Nov. 1998, pp. 1132–1135.

[49] Z. Yu, L. Fu, D. Pal, J.-B. Thibault, C. A. Bouman, and K. D. Sauer, "Nested loop algorithm for parallel model based iterative reconstruction," in *Proc. Int. Meeting Fully 3D Image Reconstruction Radiol. Nucl. Med.*, 2013, pp. 197–200.

[50] L. Fu, Z. Yu, J.-B. Thibault, B. De Man, M. G. McGaffin, and J. A. Fessler, "Space-variant channelized preconditioner design for 3D iterative CT reconstruction," in *Proc. Int. Meeting Fully 3D Image Reconstruction Radiol. Nucl. Med.*, 2013, pp. 205–208.

[51] B. De Man and S. Basu, "Distance-driven projection and backprojection in three dimensions," *Phys. Med. Biol.*, vol. 49, no. 11, pp. 2463–2475, 2004.